

# Modeling Human Preference and Stochastic Error for Medical Image Segmentation with Multiple Annotators

Zehui Liao<sup>\*,1</sup>, Shishuai Hu<sup>\*,1</sup>, Yutong Xie<sup>1,2</sup>, and Yong Xia<sup>†,1</sup>

<sup>1</sup>School of Computer Science and Engineering, Northwestern Polytechnical University, China

<sup>2</sup>The University of Adelaide, Australia

{merrical, sshu}@mail.nwpu.edu.cn; yutong.xie678@gmail.com; yxia@nwpu.edu.cn

## Abstract

*Manual annotation of medical images is highly subjective, leading to inevitable and huge annotation biases. Deep learning models may surpass human performance on a variety of tasks, but they may also mimic or amplify these biases. Although we can have multiple annotators and fuse their annotations to reduce stochastic errors, we cannot use this strategy to handle the bias caused by annotators' preferences. In this paper, we highlight the issue of annotator-related biases on medical image segmentation tasks, and propose a Preference-involved Annotation Distribution Learning (PADL) framework to address it from the perspective of disentangling an annotator's preference from stochastic errors using distribution learning so as to produce not only a meta segmentation but also the segmentation possibly made by each annotator. Under this framework, a stochastic error modeling (SEM) module estimates the meta segmentation map and average stochastic error map, and a series of human preference modeling (HPM) modules estimate each annotator's segmentation and the corresponding stochastic error. We evaluated our PADL framework on two medical image benchmarks with different imaging modalities, which have been annotated by multiple medical professionals, and achieved promising performance on all five medical image segmentation tasks.*

## 1. Introduction

Medical image segmentation plays a crucial role in delivering effective patient care in diagnostic and treatment practices. Among numerous segmentation approaches, deep convolutional neural networks (CNNs) have recently become the de facto standard, providing the state-of-the-art (SOTA) performance on many segmentation tasks [11, 24, 38, 40]. Known as data-driven techniques, CNNs require a large scale of accurately annotated images for training,

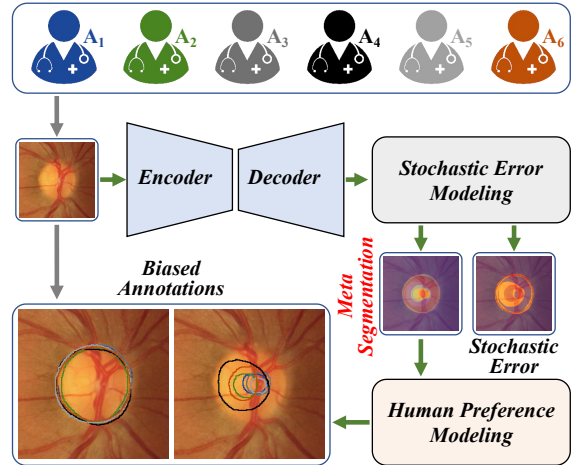


Figure 1. Modeling annotation bias in medical image segmentation using the proposed PADL framework. Based on their perceptions and expertise, multiple annotators give inconsistent annotations of the same fundus image (indicated by gray arrows). The pipeline of proposed PADL framework is highlighted by green arrows. Under this framework, the meta segmentation map is disentangled from the stochastic error via establishing the annotation distribution, and the annotation made by each annotator (with personal preference) is then predicated based on the meta segmentation map and image features.

which is indeed impossible to obtain on medical image segmentation tasks. Besides its tremendous cost, manual annotation of medical images can hardly be *accurate*, since it is highly subjective and relies on observers' perception and expertise [6, 23, 26, 31]. For example, three trained observers (two radiologists and one radiotherapist) delineated a lesion of the liver in an abdominal CT image twice with an interval of about one week, resulting in the variation of delineated areas up to 10% per observer and more than 20% between observers<sup>1</sup> [30]. The annotator-related bias in ground truths is an 'inconvenient truth' in the field of medical image seg-

<sup>\*</sup>Equal contribution.

<sup>1</sup>See the figure in this page.

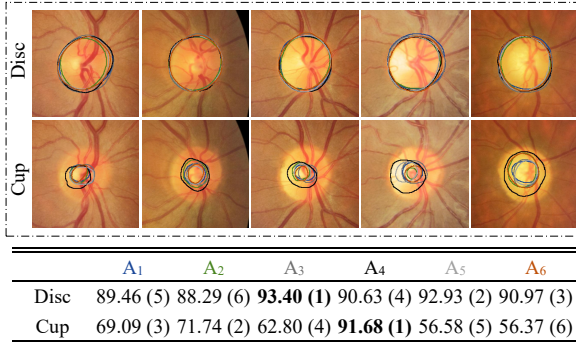


Figure 2. Annotator preference counted from the training set of RIGA. There are five fundus images annotated by six annotators. The IoU between each annotation and the union of six annotations is utilized to quantify the annotator preference. The table shows the average IoU of all training samples. The number in brackets is the rank from highest to lowest in each row.

mentation, whose impact has been rarely discussed.

To reduce the impact of such annotator-related biases, each training sample can be annotated by multiple medical professionals independently [6, 23, 26, 31] (see Figure 1), and a proxy ground truth is generated via majority voting [9], label fusion [3, 22, 24, 35, 43, 44], or label sampling [13]. It is worth noting that, in many cases, the variable annotations provided by multiple annotators are all reasonable. For instance, a medical professional who advocates for active treatment usually delineates a slightly larger area of a lesion than the area marked by others. To illustrate the annotator’s preference, we show five fundus images from the RIGA dataset and the annotations of optic disc and optic cup given by six annotators in Figure 2. The IoU of each annotator’s delineation over the union of six annotations is calculated, and the average IoU values over all training samples are listed at the bottom of this figure. It reveals that the annotator  $A_3$  prefers to mark much larger optic discs, and the annotator  $A_4$  and  $A_2$  prefer to mark larger optic cups. Using proxy ground truths can somehow diminish the impact of stochastic annotation errors [27, 28], but cannot tackle the annotator’s preference [9, 14, 21, 27, 29]. Particularly, converting the multiple annotations of each training image into a proxy ground truth not only overlooks the rich information embedded in those annotations, but, more important, may lead the segmentation result to be neither fish nor fowl. Therefore, instead of reducing the impact of annotation differences, we advocate to disentangle annotators’ preference from stochastic annotation errors and characterize both statistically so that a CNN is able to not only produce objective image segmentation, namely meta segmentation, but also mimic each annotator and segment medical images with his or her preference (see Figure 1).

To this end, we propose a Preference-involved Annota-

tion Distribution Learning (PADL) framework to address the issue of annotator-related bias in medical image segmentation. Under this framework, there are an encoder-decoder backbone, a stochastic error modeling (SEM) module, a series of human preference modeling (HPM) modules, and a series of Gaussian Sampling modules. The backbone performs feature extraction. The SEM module uses image features to estimate the meta segmentation map  $\mu$  and average stochastic error map  $\sigma$  via annotation distribution approximation. This module also contains an entropy guided attention (EGA) block, where the entropy map of  $\mu$  serves as the attention to guide the estimation of  $\sigma$ . In the  $r$ -th HPM module, a preference estimation block uses the combination of meta segmentation and image features to estimate the  $r$ -th annotator’s segmentation map  $\mu_r$ , and an EGA block estimates the corresponding stochastic error map  $\sigma_r$ . The SEM module and each HPM module is equipped with a Gaussian Sampling module, which samples a probabilistic segmentation map from the Gaussian distribution established by the estimated  $\mu$  (or  $\mu_r$ ) and  $\sigma$  (or  $\sigma_r$ ). The loss function is composed of the meta segmentation loss and annotator-specific segmentation loss, each being defined as the binary cross-entropy loss between the sampled segmentation maps and annotations. We have evaluated the proposed PADL framework on two medical image segmentation benchmarks, which include multiple imaging modalities and five segmentation tasks and are annotated by multiple medical professionals. To summarise, the contributions of this work are three-fold.

- We highlight the issue of annotator-related biases existed in medical image segmentation tasks, and propose the PADL framework to address it from the perspective of disentangling an annotator’s preference from stochastic errors so as to produce not only a meta segmentation but also the segmentation possibly made by each annotator.
- We treat the annotation bias as the combination of an annotator’s preference and stochastic errors, and hence design the SEM module and annotator-specific HPM module to characterize each annotator’s preference while diminishing the impact of stochastic errors.
- Our PADL framework achieves superior performance against other methods tackling this issue on two medical image segmentation benchmarks (five tasks) with multiple annotators.

## 2. Related Work

### Medical Image Segmentation with Multiple Annotators.

A few methods have been proposed to address the issue of annotator-related bias in medical image segmentation, which can be roughly grouped into two categories. *Annotator decision fusion methods* usually use multiple convo-

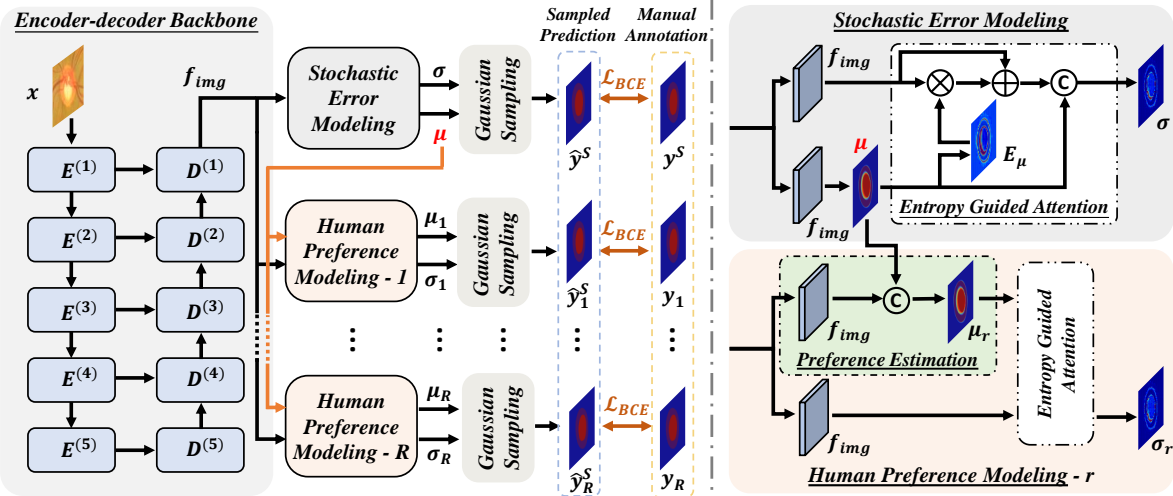


Figure 3. Architecture of PADL framework. Our PADL contains an encoder-decoder backbone, a SEM module,  $R$  HPM modules, and  $R + 1$  Gaussian Sampling modules, where  $\hat{y}^S$  (or  $\hat{y}_r^S$ ) represents the randomly sampled prediction from  $\mathcal{N}(\mu, \sigma^2)$  (or  $\mathcal{N}(\mu_r, \sigma_r^2)$ ),  $y_r$  denotes the annotation from  $r$ -th annotator,  $y^S$  is the randomly sampled annotation from  $R$  annotators,  $R$  is the number of annotators,  $\mu$  and  $\mu_r$  are the meta segmentation and the  $r$ -th annotator's preference-involved segmentation, and  $\sigma$  and  $\sigma_r$  are the average stochastic error and annotator-specific stochastic error. The SEM module is shown at top right, and the HPM module is shown at bottom right, where  $\odot$ ,  $\oplus$ , and  $\otimes$  denote the concatenation, element-wise addition, and element-wise multiplication, respectively, and  $E_\mu$  means the entropy of  $\mu$ . Note that only the  $r$ -th HPM module is shown due to the space limit.

lutional heads to model annotators, respectively, and calculate weighted sum of multi-head outputs as the segmentation result [27, 37]. Recently, the uncertainty map that measures the disagreements among all annotators has been adopted as the spatial attention to calibrate the segmentation result [14]. Despite their advantages, these methods are sensitive to stochastic annotation errors [15]. With the advance of image classification using noisy labels [32], *an annotator bias disentangling method* that uses two coupled CNNs has been proposed to disengage annotator bias from these inconsistent annotations [41, 42]. The segmentation CNN estimates the label distribution, and the annotation CNN models the human bias using a confusion matrix. Although achieving promising performance under elaborated hyper parameters, this method cannot estimate the expected label distribution effectively due to the undesired constraint of the confusion matrix. By contrast, our PADL establishes the annotation distribution to disentangle the operator's preference from stochastic errors. The preference is modeled as a series of annotation transformations using a stack of convolution layers.

**Annotation Distribution Learning.** The research on annotation distribution learning can be traced back to the seminal work of probabilistic U-Net (PU-Net) [19], which combines a U-Net [5] with a conditional variational autoencoder (VAE) to form a generative segmentation model that is able to produce an unlimited number of plausible segmentation results. Thanks to the development of VAE and repara-

terization [18], annotation distribution learning has recently been increasingly studied [2, 12, 16, 19, 20]. Hierarchical Probabilistic U-Net [20] was constructed to improve the segmentation reconstruction fidelity by introducing a hierarchical latent space decomposition. An adversarial refinement method [16] was proposed for stochastic semantic segmentation, which employs a generative adversarial network [7] to calibrate the predicted distribution over semantic maps. These methods model the distribution at the feature level. By contrast, our PADL employs annotation distribution learning to directly approximate the distribution from the biased annotations at the output level so that the impact of stochastic errors can be diminished. Furthermore, we model human preference as annotation transformations so as to further reconstruct each annotator's segmentation.

### 3. Method

#### 3.1. Problem Definition and Method Overview

Let a set of medical image annotated by  $R$  annotators be denoted by  $D = \{x_i, y_{i1}, y_{i2}, \dots, y_{iR}\}_{i=1}^N$ , where  $x_i \in \mathbb{R}^{C \times H \times W}$  represents the  $i$ -th image with  $C$  channels and a size of  $H \times W$ , and  $y_{ir} \in \{0, 1\}^{K \times H \times W}$  is the annotation with  $K$  classes given by the  $r$ -th annotator. Our goal is to train a segmentation model on the training set  $D_{tr}$  so that the model can mimic each annotator and perform segmentation on the testing set  $D_{ts}$  with his/her preference.

The proposed PADL framework consists of an encoder-decoder backbone, a SEM module,  $R$  HPM modules, and

$R + 1$  Gaussian Sampling modules (see Fig. 3). For each input image  $x$ , the backbone extracts its feature map  $f_{img}$ . Based on  $f_{img}$ , the SEM module estimates a meta segmentation map  $\mu$ , which approximates the mean voting of  $R$  annotations, and an average stochastic error map  $\sigma$ . Based on  $\mu$  and  $f_{img}$ , a HPM module can estimate the segmentation map and stochastic error map of each annotator, denoted by  $\mu_r$  and  $\sigma_r$ , respectively. With the established distributions, the Gaussian Sampling module can sample a segmentation result, which is compared with the corresponding annotation to generate the supervisory signal. We now delve into the details of our PADL framework.

### 3.2. Backbone

The backbone network has a U-like encoder-decoder structure [5], where we adopt the ResNet34 [10] pretrained on the ImageNet dataset [4] as the encoder. To adapt it to our tasks, we replace the last average pooling layer and fully connection layer in ResNet34 with a ReLU layer. Skip connections are from the convolutional block and first three residual blocks in the encoder to the corresponding locations in the decoder [14].

Symmetrically, the decoder is composed of five blocks, which upsample the feature map gradually to restore its resolution. In each of the first four blocks, the feature map is upsampled by a transposed convolutional layer with a stride of 2, processed by a convolutional layer, concatenated with the feature map from the encoder, and fed to a ReLU layer and a batch normalization layer. The last decoder block only upsamples the image features using a transposed convolutional layer with a stride of 2. As a result, the decoder produces a 32-channel feature map  $f_{img}$  for each input image, shown as follows

$$f_{img} = F_D(F_E(x; \theta_E); \theta_D), \quad (1)$$

where  $\theta_E$  and  $\theta_D$  represent the parameters in the encoder  $F_E$  and decoder  $F_D$ , respectively.

### 3.3. Stochastic Error modeling

We assume the annotation distribution to be Gaussian. To approximate this distribution, we need estimate the mean  $\mu \in \mathbb{R}^{K \times H \times W}$  and standard deviation  $\sigma \in \mathbb{R}^{K \times H \times W}$  on a pixel-by-pixel basis. When using all annotations,  $\mu$  is an estimation of the mean voting of  $R$  annotations, and hence is called the meta segmentation map. The average stochastic error existed in all annotations is measured by  $\sigma$ .

We use a  $\mu$  head  $F_\mu$ , which is a  $1 \times 1$  convolutional layer, to estimate  $\mu$  as follows

$$\mu = F_\mu(f_{img}; \theta_\mu), \quad (2)$$

where  $\theta_\mu$  represents the parameters in  $F_\mu$ .

We use a  $\sigma$  head  $F_\sigma$ , which is composed of a  $1 \times 1$  convolutional layer, a batch normalization layer and a ReLU layer, to produce the  $\sigma$  features  $f_\sigma$  as follows

$$f_\sigma = F_\sigma(f_{img}; \theta_\sigma), \quad (3)$$

where  $\theta_\sigma$  represents the parameters in  $F_\sigma$ .

**EGA Block.** The stochastic annotation errors always occur in ambiguous regions, where the entropy of manual annotations is high [16]. Therefore, we design an EGA block to process and calibrate  $f_\sigma$ .

Given the meta segmentation map  $\mu$ , its entropy map  $E_\mu$  can be calculated as

$$E_\mu = -\mu \times \log_2(\mu) - (1 - \mu) \times \log_2(1 - \mu). \quad (4)$$

We use the entropy map  $E_\mu$  as the spatial attention [36] to highlight ambiguous regions. Thus,  $f_\sigma$  can be calibrated as

$$\tilde{f}_\sigma = f_\sigma \times (1 + E_\mu). \quad (5)$$

Since the stochastic error  $\sigma$  is highly related to the meta segmentation  $\mu$ , we concatenate  $\mu$  with  $\tilde{f}_\sigma$  to predict  $\sigma$ , shown as follows

$$\sigma = F_\sigma^o((\mu \odot \tilde{f}_\sigma); \theta_\sigma^o), \quad (6)$$

where  $\odot$  represents concatenation,  $F_\sigma^o$  is a  $1 \times 1$  convolutional layer, and  $\theta_\sigma^o$  denotes the parameters in  $F_\sigma^o$ .

### 3.4. Human Preference Modeling

We design  $R$  HPM modules to characterize the preference of  $R$  annotators, respectively. Each HPM module contains a preference estimation block and an EGA block. The former estimates the annotator-specific segmentation map  $\mu_r$ , and the latter estimates the annotator-specific stochastic error  $\sigma_r$ .

**Preference Estimation.** Due to the annotator's preference, some delineated areas are larger than others and some are smaller, which can be mimicked by using morphological dilation or erosion. Inspired by this, the preference estimation block is implemented as a stack of convolutional layers. Here, we use two  $3 \times 3$  convolutional layers with a padding of 1 due to the trade-off between optimization complexity and preference modeling capacity (see ablation study in Table 5). We first use a  $1 \times 1$  convolutional layer with batch normalization and ReLU activation, denoted by  $F_p^r$ , to reduce the channel of feature map  $f_{img}$  to  $K$ . Then, we concatenate the channel-reduced feature map with meta segmentation  $\mu$ , and feed the concatenation to the preference estimation block  $F_\mu^r$  for the estimation of preference-involved segmentation map  $\mu_r$ , shown as follows

$$\mu_r = F_\mu^r((\mu \odot F_p^r(f_{img}; \theta_p^r)); \theta_\mu^r), \quad (7)$$

where  $\theta_p^r$  and  $\theta_\mu^r$  represents the parameters in  $F_p^r$  and  $F_\mu^r$ , respectively.

Since the stochastic error occurs in each annotator’s delineations, we also use the EGA block to estimate the annotator-specific stochastic error  $\sigma_r$ .

### 3.5. Gaussian Sampling

With the Gaussian assumption and estimated  $\mu$  and  $\sigma$ , the probabilistic segmentation map  $\hat{y}^s$  can be sampled from the distribution  $\mathcal{N}(\mu, \sigma^2)$  on a pixel-by-pixel basis. Then, we use the sigmoid function to map those sample values to  $(0, 1)$  and normalize them to be probabilities. The probabilistic meta segmentation map  $\hat{y}$  is calculated by applying the sigmoid function to the estimated  $\mu$  followed by normalization.

Similarly, the annotator-specific segmentation prediction maps  $\{\hat{y}_r\}_{r=1}^R$  and corresponding sampled prediction maps  $\{\hat{y}_r^s\}_{r=1}^R$  can be obtained via applying sigmoid function to the preference-involved segmentation map  $\{\mu_r\}_{r=1}^R$  and the probabilistic segmentation map sampled from the established distribution  $\{\mathcal{N}(\mu_r, \sigma_r^2)\}_{r=1}^R$ .

### 3.6. Loss and Inference

**Loss.** The loss of our PADL framework consists of two parts: the meta segmentation loss  $\mathcal{L}_{meta}$  and annotator-specific segmentation loss  $\mathcal{L}_{pref}$ , shown as follows

$$\mathcal{L} = \mathcal{L}_{meta}(y^s, \hat{y}^s) + \sum_{r=1}^R \mathcal{L}_{pref}(y_r, \hat{y}_r^s), \quad (8)$$

where  $y^s$  is randomly selected from all annotations per image,  $y_r$  is the delineation given by annotator  $A_r$ , and the meta segmentation loss is the following binary cross-entropy loss

$$\mathcal{L}_{meta}(y^s, \hat{y}^s) = -y^s \times \log \hat{y}^s - (1 - y^s) \times \log (1 - \hat{y}^s). \quad (9)$$

The annotator-specific segmentation loss  $\mathcal{L}_{pref}$  is also the binary cross-entropy loss and is calculated in a similar way.

**Inference.** During inference, the estimated  $\mu$  in the SEM module is adopted as meta segmentation, and the probability map  $\hat{y}$  is used to evaluate with mean voting annotation  $\bar{y}$ . The approximated  $\mu_r$  in each HPM module is viewed as the predicted annotator-specific segmentation map involving human preference, and its corresponding probability map  $\hat{y}_r$  is utilized to measure the similarity with delineation  $y_r$  from annotator  $A_r$ .

## 4. Experiments

### 4.1. Datasets

**The RIGA dataset** [1] is collected for the evaluation of optic cup and optic disc segmentation algorithms. It contains 750 color fundus images from three sources, including 460 images from MESSIDOR, 195 images from Bin-Rushed, and 95 images from Magribia. Six ophthalmologists from different eye centers labeled the optic cup and

disc contours manually in each image. We followed the data split scheme used in [14, 39], using 655 samples from Bin-Rushed and MESSIDOR for training and 95 samples from Magribia for test.

**The QUBIQ dataset** [25] is a dataset specifically collected to evaluate inter-annotator variability. It contains four subsets, including 39 MRI cases (34 for training and 5 for test) with seven annotators for brain growth segmentation, 32 MRI cases (28 for training and 4 for test) with three annotators for brain tumor segmentation, 55 MRI cases (48 for training and 7 for test) with six annotators for prostate and center zone segmentation, and 24 CT cases (20 for training and 4 for test) with three annotators for kidney segmentation. The dataset split was provided by [14].

### 4.2. Experimental Setup

**Implementation Details.** For each segmentation task, all images were normalized via subtracting the mean and dividing by the standard deviation on a pixel-by-pixel basis. The mean and standard deviation were counted on training cases. For a fair comparison, we followed the settings in [14], *i.e.*, setting the mini-batch size to 8 and resizing the input image to  $256 \times 256$  for all tasks. The images in the prostate subset in QUBIQ are relatively large, and hence were center cropped to  $640 \times 640$  before resizing to  $256 \times 256$ . The Adam optimizer [17] with a initial learning rate of  $lr_0 = 1e-4$  was adopted as the optimizer. The learning rate was decayed according to the polynomial policy  $lr = lr_0 \times (1 - t/T)^{0.9}$ , where  $t$  is the current epoch and  $T$  is the maximum epoch. The maximum epoch  $T$  was set to 60 for optic cup and optic disc segmentation and 1000 for QUBIQ segmentation tasks. Other parameters in Adam were set as default. All experiments were performed on a workstation with one NVIDIA RTX 2080Ti GPU and implemented under the PyTorch framework.

**Evaluation Metrics.** Since each test sample has multiple annotations, we adopted the Soft Dice ( $\mathcal{D}$ ) and Soft IoU ( $IoU$ ) as performance metrics. At each threshold level, the threshold is applied to the predicted probability map and mean voting of annotations to generate hard Dice/IoU. Soft Dice/IoU is calculated via averaging the hard Dice/IoU values obtained at multiple threshold levels, *i.e.*, (0.1, 0.3, 0.5, 0.7, 0.9) for this study. Higher soft Dice/IoU represents better segmentation performance.

### 4.3. Experimental Results

#### 4.3.1 Experiments on RIGA dataset

**Comparison Concerning Annotator-Related Bias Issue.** On the RIGA dataset, we compared our PADL to (1) the baseline ‘Multi-Net’ setting, under which six U-Nets (denoted by  $M_1 \sim M_6$ ) were trained with the annotations provided by annotator  $A_1 \sim A_6$ , respectively); (2) MH-UNet: a U-Net variant with multiple heads, each accounting for

Table 1. Performance of our PADL framework, 11 competing methods, and two variants of PADL in optic disc and optic cup segmentation on RIGA. The soft Dice ( $\mathcal{D}_{disc}^s$  (%),  $\mathcal{D}_{cup}^s$  (%)) are used as the performance metric. The predictions of each model are evaluated against each annotator’s delineations and the mean voting annotation, and the average performance over six annotations is also given. Except for the results of Multi-Net ( $M_1 \sim M_6$ ) and two PADL variants, top three results in each column are highlighted in **red**, **blue** and **green**, respectively. In each column, the best result among  $M_1 \sim M_6$  is highlighted with underline. The cells in **gray** represent the U-Nets trained and tested using the annotations from the same annotator.

Models	A <sub>1</sub>	A <sub>2</sub>	A <sub>3</sub>	A <sub>4</sub>	A <sub>5</sub>	A <sub>6</sub>	Average	Mean Voting
M <sub>1</sub>	( <u>96.16</u> , 84.29)	(95.08, 80.79)	(95.57, 79.82)	(96.29, 78.91)	(95.91, 80.49)	(96.47, 76.57)	(95.91, 80.15)	(96.27, 80.56)
M <sub>2</sub>	(95.72, 84.71)	( <u>95.50</u> , 84.20)	(95.52, 79.87)	(96.13, 81.16)	(96.13, 80.91)	(96.27, 77.93)	(95.88, <u>81.46</u> )	(96.30, 82.03)
M <sub>3</sub>	(95.10, 82.76)	(94.50, 79.69)	( <u>96.53</u> , <u>83.10</u> )	(96.20, 78.39)	(96.28, 81.47)	(95.92, 76.73)	(95.76, 80.36)	(95.89, 80.90)
M <sub>4</sub>	(95.92, 81.46)	(95.30, 82.16)	(96.18, 78.53)	( <u>96.79</u> , <u>87.90</u> )	( <u>96.84</u> , 74.47)	(96.43, 70.57)	( <u>96.24</u> , 79.18)	(96.44, 78.94)
M <sub>5</sub>	(95.27, 82.93)	(94.83, 79.99)	(96.27, 81.62)	(96.39, 75.94)	( <u>96.69</u> , <u>83.15</u> )	(95.91, 77.64)	(95.89, 80.21)	(96.08, 81.02)
M <sub>6</sub>	(95.92, 80.94)	(95.31, 78.48)	(96.23, 78.14)	(96.56, 73.62)	(96.45, 81.64)	( <u>96.90</u> , <u>80.45</u> )	(96.22, 78.88)	( <u>96.55</u> , 80.23)
MH-UNet [9]	( <b>96.36</b> , <b>83.49</b> )	( <b>95.32</b> , <b>81.84</b> )	( <b>96.75</b> , 77.20)	( <b>97.01</b> , <b>88.21</b> )	( <b>97.15</b> , 78.95)	( <b>97.22</b> , 75.85)	( <b>96.64</b> , <b>80.92</b> )	(97.41, 85.21)
MV-UNet [5]	(95.12, 76.65)	(94.57, 78.12)	(95.55, 77.74)	(95.79, 76.31)	(95.87, 78.67)	(95.68, 74.80)	(95.43, 77.05)	(97.42, <b>86.11</b> )
LS-UNet [13]	(95.43, 75.66)	(94.82, 74.56)	(95.57, 73.52)	(95.96, 72.30)	(95.90, 75.72)	(95.93, 72.85)	(95.60, 74.10)	( <b>97.58</b> , 82.68)
MR-Net [14]	(95.35, 81.77)	(94.81, 81.18)	(95.80, <b>79.23</b> )	(95.96, 84.46)	(95.90, <b>79.04</b> )	(95.76, <b>76.20</b> )	(95.60, 80.31)	( <b>97.55</b> , <b>87.20</b> )
CM-Net [42]	( <b>96.29</b> , <b>84.59</b> )	( <b>95.46</b> , <b>81.44</b> )	( <b>96.60</b> , <b>81.84</b> )	( <b>96.90</b> , <b>87.52</b> )	( <b>96.86</b> , <b>82.39</b> )	( <b>96.93</b> , <b>78.82</b> )	( <b>96.51</b> , <b>82.77</b> )	(96.64, 81.96)
Ours	( <b>96.40</b> , <b>85.22</b> )	( <b>95.60</b> , <b>85.15</b> )	( <b>96.64</b> , <b>82.76</b> )	( <b>96.82</b> , <b>88.79</b> )	( <b>96.78</b> , <b>83.45</b> )	( <b>96.87</b> , <b>79.72</b> )	( <b>96.52</b> , <b>84.18</b> )	( <b>97.65</b> , <b>87.75</b> )
Ours w/o SEM	(96.49, 84.87)	(95.69, 83.13)	(96.42, 83.70)	(96.93, 88.73)	(96.64, 81.99)	(96.77, 79.50)	(96.49, 83.65)	(96.42, 85.37)
Ours w/o HPM	(95.70, 81.62)	(95.17, 79.95)	(96.10, 79.38)	(96.43, 78.26)	(96.37, 80.01)	(96.27, 76.21)	(96.06, 79.24)	(97.71, 87.56)

imitating the annotations from a specific annotator [9]; (3) MV-UNet: a U-Net trained with the mean voting of annotations [5]; (4) LS-UNet: a U-Net trained with randomly selected annotations [13]; (5) MR-Net: an annotator decision fusion method that uses an attention module to model the multi-rater agreement [14]; and (6) CM-Net: an annotator bias disentangling method that uses a confusion matrix to model human errors [42].

The soft Dice of optic disc  $\mathcal{D}_{disc}^s$  and optic cup  $\mathcal{D}_{cup}^s$  obtained by our model and competing methods were listed in Table 1. As expected, the U-Net trained using the annotations from annotator  $A_r$  always achieves higher performance when evaluated against  $A_r$ ’s delineations, except that  $M_1$  slightly underperforms  $M_2$  in  $\mathcal{D}_{cup}^s$  and  $M_5$  slightly underperforms  $M_4$  in  $\mathcal{D}_{disc}^s$ . Also, the mean voting-based proxy ground truth method MV-UNet outperforms the multi-network ( $M_1 \sim M_6$ ) and multi-head (MH-UNet) methods when evaluated against the mean voting of annotations, but underperforms both when evaluate against each annotator’s delineations. A similar conclusion can be drawn for the random annotation-based proxy ground truth method LS-UNet, except for its surprisingly low performance in optic cup segmentation. Meanwhile, since the annotator-related bias is considered, both MR-Net and CM-Net perform well no matter being evaluated against the mean voting or each individual annotation. Between them, MR-Net outperforms CM-Net when evaluated against the mean voting, but is inferior to CM-Net in reconstructing each annotator’s delineations. It may attribute to the fact that the annotator decision fusion strategy can hardly preserve each annota-

tor’s preference. Among 12 competing methods (two variants of PADL not counted in), the proposed PADL achieves the second highest average  $\mathcal{D}_{disc}^s$  and highest average  $\mathcal{D}_{cup}^s$  when evaluated against each annotator’s delineations and achieves the highest soft Dice on both segmentation tasks when evaluated against the mean voting. It should be noted that, comparing to the annotator bias disentangling method CM-Net, our PADL is able to not only reconstruct each annotator’s delineations slightly better but also perform substantially more accurate meta segmentation to approximate the mean voting of annotations.

We visualized the probabilistic segmentation maps predicted by our PADL and other four competing methods, *i.e.*, MR-Net, CM-Net, MV-UNet and MH-UNet, and the mean voting annotation maps of four cases in Figure 4. It shows that our PADL can produce more accurate probability maps, confirming that our PADL can model the consensus among all annotators via disentangling stochastic errors from the meta segmentation.

**Comparing to SOTA Methods for Optic Cup and Disc Segmentation.** To demonstrate the effectiveness of the proposed PADL framework, we also compared it to five SOTA methods for joint optic cup and optic disc segmentation, including CENet [8], ResUNet [39], pOSAL [34], BEAL [33], and MR-Net [14]. For a fair comparison, we adopted the backbone network and data split scheme used by MR-Net [14]. Table 2 gives the soft Dice and soft IoU obtained by evaluating against the mean voting of annotations. The performance metrics of all competing methods were adopted from [14]. It reveals that our PADL outper-

Table 2. Performance of our PADL framework and five SOTA methods for optic cup and disc segmentation on RIGA.

Models	$\mathcal{D}_{disc}^s$ (%)	$\mathcal{D}_{cup}^s$ (%)	$IoU_{disc}^s$ (%)	$IoU_{cup}^s$ (%)
CENet [8]	96.55	81.82	93.38	71.03
ResUNet [39]	96.75	85.38	93.75	75.76
pOSAL [34]	95.85	84.07	92.12	74.40
BEAL [33]	97.08	85.97	94.38	77.18
MR-Net [14]	97.55	87.20	95.24	78.62
Ours	<b>97.65</b>	<b>87.75</b>	<b>95.43</b>	<b>79.36</b>

Table 3. Soft Dice (%) of our PADL framework and five competing methods obtained on five segmentation tasks using the QUBIQ dataset. The ground truth is the majority voting with average weight of annotations from multiple annotators.

Methods	$\mathcal{D}_{kidney}^s$	$\mathcal{D}_{brain}^s$	$\mathcal{D}_{tumor}^s$	$\mathcal{D}_{pros1}^s$	$\mathcal{D}_{pros2}^s$
MV-UNet [5]	70.65	81.77	84.03	85.18	68.39
LS-UNet [13]	72.31	82.79	85.85	86.23	69.05
MH-UNet [9]	73.44	83.54	86.74	87.03	75.61
MR-Net [14]	74.97	84.31	88.40	87.27	76.01
CM-Net [42]	76.01	84.75	87.37	88.73	77.39
Ours	<b>80.34</b>	<b>85.86</b>	<b>89.25</b>	<b>93.30</b>	<b>80.67</b>

forms all competitors consistently, suggesting the effectiveness of our method on these two segmentation tasks.

#### 4.3.2 Experiments on QUBIQ dataset

We conducted five CT or MRI image segmentation tasks using the QUBIQ dataset. We compared the proposed PADL with five methods, including: (1) three commonly used strategies that consider the annotator-related bias, *i.e.*, MV-UNet [5], LS-UNet [13], and MH-UNet [9], (2) two recent methods that attempt to address this issue, *i.e.*, MR-Net [14] and CM-Net [42]. Since CM-Net uses a different backbone, we replaced its backbone with the one used by other methods [14] via revising the publicly released code. We also optimized the hyper-parameters for CM-Net and adopted the same experimental settings [14] for a fair comparison. Table 3 shows the soft Dice of our PADL and five competing methods obtained by evaluating against the majority voting of annotations. Note that the soft Dice of four competing methods (except for CM-Net) were adopted from [14]. It reveals that the soft Dice values of three commonly used strategies are relatively lower than those of others, suggesting that both the proxy ground truth strategy and multi-head strategy suffer from limited performance. By contrast, our PADL achieves the highest soft Dice on all tasks, beating the proxy ground truth strategy, multi-head strategy, and two recent methods. The results displayed in this table are consistent with those obtained on the RIGA dataset, confirming the superior ability of our PADL to addressing the annotator-related bias issue.

Table 4. Soft Dice (%) of the PADL with complete SEM module and its three variants on the RIGA dataset.

Baseline	SEM module			$\mathcal{D}_{disc}^s$ (%)	$\mathcal{D}_{cup}^s$ (%)
	$\sigma$	$E_\mu$	$\mu$ prior		
✓				97.41	85.21
✓	✓			97.58	86.93
✓	✓	✓		97.65	87.45
✓	✓	✓	✓	<b>97.65</b>	<b>87.75</b>

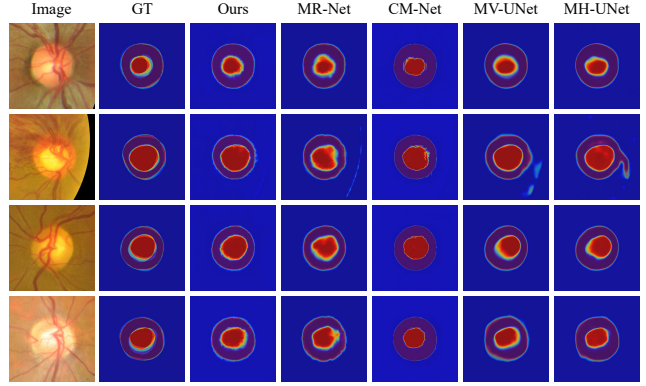


Figure 4. Visualization of probabilistic segmentation maps predicted by our PADL and four competing methods for four cases, together with ground truth (GT).

#### 4.3.3 Ablation Analysis

Both the SEM and HPM modules play an essential role in the proposed PADL framework, modeling the stochastic errors and annotators' preference independently. We conducted ablation studies on the RIGA dataset to investigate the effectiveness of these two modules, respectively.

**Contributions of SEM and HPM.** To evaluate the contributions of SEM and HPM, we compared the proposed PADL framework with its variants that use only one module, *i.e.*, ‘Ours w/o SEM’ and ‘Ours w/o HPM’. In ‘Ours w/o SEM’, the SEM module is replaced with a vanilla segmentation head, which directly converts image features to a segmentation map. Accordingly, the  $\sigma$  head in each HPM module is also removed. ‘Ours w/o HPM’ represents the variant that removes all HPM modules. This variant is, of course, not able to model the preference of each annotator. The performance of our PADL and its two variants was given in Table 1. It shows that, when the HPM modules were removed, the performance in reconstructing each annotator's delineations drops seriously, especially in optic cup segmentation, *i.e.*, the average  $\mathcal{D}_{cup}^s$  over six annotations drops remarkably from 84.18% to 79.24%. However, if we evaluated them against the mean voting annotations, the performance only decreases slightly, indicating again that the HPM module is essential for annotators' preference

Table 5. Performance (average  $\mathcal{D}_{disc}^s$  (%),  $\mathcal{D}_{cup}^s$  (%)) obtained by evaluating against six annotations of the PADL with different designs of preference estimation block  $F_\mu^r$  or different input of HPM module on the RIGA dataset. The best results in each block are highlighted in **bold**.

Models		Average
$F_\mu^r$	1 Layer $1 \times 1$ Conv	(63.13, 40.30)
	1 Layer $3 \times 3$ Conv	(96.55, 83.21)
	1 Layer $5 \times 5$ Conv	<b>(96.66, 82.93)</b>
	2 Layers $3 \times 3$ Conv	(96.52, <b>84.18</b> )
	3 Layers $3 \times 3$ Conv	(96.61, 82.45)
HPM w/o $f_{img}$		(96.40, 83.39)
HPM w/o $\mu$		(95.95, 80.22)
HPM		<b>(96.52, 84.18)</b>

independently. Meanwhile, it also shows that, without the SEM module, the performance of consensus reconstruction drops from 97.65% to 96.42% for optic disc segmentation and from 87.75% to 85.37% for optic cup segmentation. When evaluating with each annotator’s delineations, the average performance decline in optic cup segmentation can also be observed, *i.e.*, from 84.18% to 83.65%. These results indicate that HPM modules contribute a lot to the reconstruction of each annotator’s preference, and the SEM module can effectively diminish the impact of stochastic errors and produce accurate consensus reconstruction.

**Analysis of Stochastic Error Modeling.** The effect of each block in the SEM module was accessed using the mean voting annotations as the ground truth. Table 4 gives the performance of the PADL with complete SEM module and its three variants. It shows that the stochastic error modeling strategy improves  $\mathcal{D}_{disc}^s$  and  $\mathcal{D}_{cup}^s$  by 0.17% and 1.72% respectively, suggesting the necessity of error disentangling from manual annotations. It also reveals that the entropy attention and the meta segmentation prior can further improve  $\mathcal{D}_{cup}^s$  by 0.52% and 0.3%, respectively. It verifies that the proposed EGA block can emphasize the regions where stochastic errors are prone to happen and improve the capacity of stochastic error modeling. In Figure 5, we visualized the meta segmentation maps and stochastic error maps obtained by applying PADL to seven cases, together with the mean voting annotations. It shows that our PADL framework can model the stochastic error efficiently and thus produces accurate meta segmentation results.

**Analysis of Human Preference Modeling.** The HPM module uses the preference estimation block to reconstruct an annotator’s preference based on both image features and the meta segmentation. We attempted different designs of the preference estimation block, ranging from a  $1 \times 1$  convolutional layer to three  $3 \times 3$  convolutional layers, and also tested the HPM module using either image features or meta segmentation as its input. The average  $\mathcal{D}_{disc}^s$  and  $\mathcal{D}_{cup}^s$  eval-

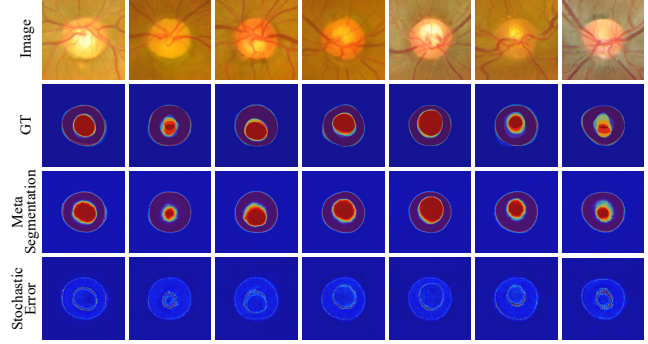


Figure 5. Visualization of estimated meta segmentation and stochastic error of seven cases from the RIGA dataset.

uated against each annotator’s delineations over six annotators were displayed in Table 5. It shows that the preference estimation block  $F_\mu^r$  with two of  $3 \times 3$  convolutional layers achieves substantially better  $\mathcal{D}_{cup}^s$  than that of other settings. It seems that  $1 \times 1$  kernels cannot model human preference due to its small perception field and  $5 \times 5$  kernels can improve the perception field, but may miss fine details. Moreover, the performance of the deeper design (with three layers) is limited by the increased optimization difficulty. Meanwhile, when the meta segmentation  $\mu$  is removed from the input, the performance on  $\mathcal{D}_{cup}^s$  drops remarkably from 84.18% to 80.22%, suggesting that the meta segmentation plays a more important role than image features  $f_{img}$  in annotator preference estimation. It can be attributed to the fact that the meta segmentation contains rich-semantic consensus information and is able to enhance the perception of the preference estimation. Without the meta segmentation, each preference estimation head has to reconstruct each annotator’s delineation from scratch based merely on  $f_{img}$ , which is hard to achieve.

## 5. Conclusion

In this work, we highlight the issue of annotator-related biases existed in the field of medical image segmentation and propose the PADL framework, which treats the annotation bias as the combination of annotator’s preference and stochastic errors, and hence design the SEM module and annotator-specific HPM modules to characterize each annotator’s preference while diminishing the impact of stochastic errors. To our best knowledge, this is the first work that simultaneously explicitly models the annotator preference and disentangles the stochastic annotation error by learning the annotation distribution. Experimental results on two medical image segmentation benchmarks show that our PADL framework performs well on modeling human preference and disentangling stochastic errors, and achieves better performance against other methods for medical image segmentation with biased annotations.

## References

[1] Ahmed Almazroa, Sami Alodhayb, Essameldin Osman, Es-lam Ramadan, Mohammed Hummadi, Mohammed Dlaim, Muhamnad Alkatee, Kaamran Raahemifar, and Vasudevan Lakshminarayanan. Agreement among ophthalmologists in marking the optic disc and optic cup in fundus images. *International Ophthalmology*, 37(3):701–717, 2017. 5

[2] Christian F Baumgartner, Kerem C Tezcan, Krishna Chaitanya, Andreas M Hötker, Urs J Muehlematter, Khoshy Schawkat, Anton S Becker, Olivio Donati, and Ender Konukoglu. PhiSeg: Capturing uncertainty in medical image segmentation. In *International Conference on Medical Image Computing and Computer-Assisted Intervention*, pages 119–127. Springer, 2019. 3

[3] Geng Chen, Dehui Xiang, Bin Zhang, Haihong Tian, Xiaolong Yang, Fei Shi, Weifang Zhu, Bei Tian, and Xinjian Chen. Automatic pathological lung segmentation in low-dose CT image using eigenspace sparse shape composition. *IEEE Transactions on Medical Imaging*, 38(7):1736–1749, 2019. 2

[4] Jia Deng, Wei Dong, Richard Socher, Li-Jia Li, Kai Li, and Li Fei-Fei. Imagenet: A large-scale hierarchical image database. In *Proceedings of the IEEE/CVF Conference on Computer Vision and Pattern Recognition*, pages 248–255. Ieee, 2009. 4

[5] Thorsten Falk, Dominic Mai, Robert Bensch, Özgür Çiçek, Ahmed Abdulkadir, Yassine Marrakchi, Anton Böhm, Jan Deubner, Zoe Jäckel, Katharina Seiwald, et al. U-Net: Deep learning for cell counting, detection, and morphometry. *Nature Methods*, 16(1):67–70, 2019. 3, 4, 6, 7

[6] Michael C Fu, Rafael A Buerba, William D Long III, Daniel J Blizzard, Andrew W Lischuk, Andrew H Haims, and Jonathan N Grauer. Interrater and intrarater agreements of magnetic resonance imaging findings in the lumbar spine: Significant variability across degenerative conditions. *The Spine Journal*, 14(10):2442–2448, 2014. 1, 2

[7] Ian Goodfellow, Jean Pouget-Abadie, Mehdi Mirza, Bing Xu, David Warde-Farley, Sherjil Ozair, Aaron Courville, and Yoshua Bengio. Generative adversarial nets. *Advances in Neural Information Processing Systems*, 27, 2014. 3

[8] Zaiwang Gu, Jun Cheng, Huazhu Fu, Kang Zhou, Huaying Hao, Yitian Zhao, Tianyang Zhang, Shenghua Gao, and Jiang Liu. CE-Net: Context encoder network for 2D medical image segmentation. *IEEE Transactions on Medical Imaging*, 38(10):2281–2292, 2019. 6, 7

[9] Melody Guan, Varun Gulshan, Andrew Dai, and Geoffrey Hinton. Who said what: Modeling individual labelers improves classification. In *Proceedings of the AAAI Conference on Artificial Intelligence*, volume 32, 2018. 2, 6, 7

[10] Kaiming He, Xiangyu Zhang, Shaoqing Ren, and Jian Sun. Deep residual learning for image recognition. In *Proceedings of the IEEE/CVF Conference on Computer Vision and Pattern Recognition*, pages 770–778, 2016. 4

[11] Shishuai Hu, Zehui Liao, Jianpeng Zhang, and Yong Xia. Domain and content adaptive convolution for domain generalization in medical image segmentation. *arXiv preprint arXiv:2109.05676*, 2021. 1

[12] Shi Hu, Daniel Worrall, Stefan Knegt, Bas Veeling, Henkjan Huisman, and Max Welling. Supervised uncertainty quantification for segmentation with multiple annotations. In *International Conference on Medical Image Computing and Computer-Assisted Intervention*, pages 137–145. Springer, 2019. 3

[13] Martin Holm Jensen, Dan Richter Jørgensen, Raluca Jalaboi, Mads Eiler Hansen, and Martin Aastrup Olsen. Improving uncertainty estimation in convolutional neural networks using inter-rater agreement. In *International Conference on Medical Image Computing and Computer-Assisted Intervention*, pages 540–548. Springer, 2019. 2, 6, 7

[14] Wei Ji, Shuang Yu, Junde Wu, Kai Ma, Cheng Bian, Qi Bi, Jingjing Li, Hanruo Liu, Li Cheng, and Yefeng Zheng. Learning calibrated medical image segmentation via multi-rater agreement modeling. In *Proceedings of the IEEE/CVF Conference on Computer Vision and Pattern Recognition*, pages 12341–12351, 2021. 2, 3, 4, 5, 6, 7

[15] Alain Jungo, Raphael Meier, Ekin Ermis, Marcela Blatti-Moreno, Evelyn Herrmann, Roland Wiest, and Mauricio Reyes. On the effect of inter-observer variability for a reliable estimation of uncertainty of medical image segmentation. In *International Conference on Medical Image Computing and Computer-Assisted Intervention*, pages 682–690. Springer, 2018. 3

[16] Elias Kassapis, Georgi Dikov, Deepak K. Gupta, and Cedric Nugteren. Calibrated adversarial refinement for stochastic semantic segmentation. In *Proceedings of the IEEE/CVF International Conference on Computer Vision*, pages 7057–7067, October 2021. 3, 4

[17] Diederik P Kingma and Jimmy Ba. Adam: A method for stochastic optimization. In *International Conference on Learning Representations*, 2015. 5

[18] Diederik P Kingma and Max Welling. Auto-encoding variational bayes. In *International Conference on Learning Representations*, 2014. 3

[19] Simon Kohl, Bernardino Romera-Paredes, Clemens Meyer, Jeffrey De Fauw, Joseph R Ledsam, Klaus Maier-Hein, SM Eslami, Danilo Jimenez Rezende, and Olaf Ronneberger. A probabilistic u-net for segmentation of ambiguous images. *Advances in Neural Information Processing Systems*, 31, 2018. 3

[20] Simon AA Kohl, Bernardino Romera-Paredes, Klaus H Maier-Hein, Danilo Jimenez Rezende, SM Eslami, Pushmeet Kohli, Andrew Zisserman, and Olaf Ronneberger. A hierarchical probabilistic u-net for modeling multi-scale ambiguities. *arXiv preprint arXiv:1905.13077*, 2019. 3

[21] Thomas A Lampert, André Stumpf, and Pierre Gançarski. An empirical study into annotator agreement, ground truth estimation, and algorithm evaluation. *IEEE Transactions on Image Processing*, 25(6):2557–2572, 2016. 2

[22] Ge Li, Changsheng Li, Chan Zeng, Peng Gao, and Guotong Xie. Region focus network for joint optic disc and cup segmentation. In *Proceedings of the AAAI Conference on Artificial Intelligence*, volume 34, pages 751–758, 2020. 2

[23] Zehui Liao, Yutong Xie, Shishuai Hu, and Yong Xia. Learning from ambiguous labels for lung nodule malignancy prediction. *arXiv preprint arXiv:2104.11436*, 2021. 1, 2

[24] Quande Liu, Qi Dou, Lequan Yu, and Pheng Ann Heng. MS-Net: Multi-site network for improving prostate segmentation with heterogeneous mri data. *IEEE Transactions on Medical Imaging*, 39(9):2713–2724, 2020. 1, 2

[25] Bjoern Menze, Leo Joskowicz, Spyridon Bakas, Andras Jakab, Ender Konukoglu, Anton Becker, Amber Simpson, and Richard Do. Quantification of Uncertainties in Biomedical Image Quantification 2021, Mar. 2021. 5

[26] Zahra Mirikhraj, Kumar Abhishek, Saeed Izadi, and Ghassan Hamarneh. D-LEMA: Deep learning ensembles from multiple annotations-application to skin lesion segmentation. *Proceedings of the IEEE/CVF Conference on Computer Vision and Pattern Recognition Workshops*, pages 1837–1846, 2021. 1, 2

[27] Zahra Mirikhraj, Yiqi Yan, and Ghassan Hamarneh. Learning to segment skin lesions from noisy annotations. In *Domain Adaptation and Representation Transfer and Medical Image Learning with Less Labels and Imperfect Data*, pages 207–215. Springer, 2019. 2, 3

[28] Miguel Monteiro, Loïc Le Folgoc, Daniel Coelho de Castro, Nick Pawlowski, Bernardo Marques, Konstantinos Kamnitsas, Mark van der Wilk, and Ben Glocker. Stochastic segmentation networks: Modelling spatially correlated aleatoric uncertainty. *Advances in Neural Information Processing Systems*, 2020. 2

[29] Vinicius Ribeiro, Sandra Avila, and Eduardo Valle. Handling inter-annotator agreement for automated skin lesion segmentation. *arXiv preprint arXiv:1906.02415*, 2019. 2

[30] Paul Suetens. Fundamentals of medical imaging, 3rd edition. 2017. 1

[31] Saeid Asgari Taghanaki, Noirin Duggan, Hillgan Ma, Xinchi Hou, Anna Celler, Francois Benard, and Ghassan Hamarneh. Segmentation-free direct tumor volume and metabolic activity estimation from pet scans. *Computerized Medical Imaging and Graphics*, 63:52–66, 2018. 1, 2

[32] Ryutaro Tanno, Ardavan Saeedi, Swami Sankaranarayanan, Daniel C Alexander, and Nathan Silberman. Learning from noisy labels by regularized estimation of annotator confusion. In *Proceedings of the IEEE/CVF Conference on Computer Vision and Pattern Recognition*, pages 11244–11253, 2019. 3

[33] Shujun Wang, Lequan Yu, Kang Li, Xin Yang, Chi-Wing Fu, and Pheng-Ann Heng. Boundary and entropy-driven adversarial learning for fundus image segmentation. In *International Conference on Medical Image Computing and Computer-Assisted Intervention*, pages 102–110. Springer, 2019. 6, 7

[34] Shujun Wang, Lequan Yu, Xin Yang, Chi-Wing Fu, and Pheng-Ann Heng. Patch-based output space adversarial learning for joint optic disc and cup segmentation. *IEEE Transactions on Medical Imaging*, 38(11):2485–2495, 2019. 6, 7

[35] Simon K Warfield, Kelly H Zou, and William M Wells. Simultaneous truth and performance level estimation (STAPLE): An algorithm for the validation of image segmentation. *IEEE Transactions on Medical Imaging*, 23(7):903–921, 2004. 2

[36] Sanghyun Woo, Jongchan Park, Joon-Young Lee, and In So Kweon. CBAM: Convolutional block attention module. In *Proceedings of the European Conference on Computer Vision*, pages 3–19, 2018. 4

[37] Li Xiao, Yinhao Li, Luxi Qv, Xinxia Tian, Yijie Peng, and S Kevin Zhou. Pathological image segmentation with noisy labels. *arXiv preprint arXiv:2104.02602*, 2021. 3

[38] Yanchao Yang and Stefano Soatto. FDA: Fourier domain adaptation for semantic segmentation. In *Proceedings of the IEEE/CVF Conference on Computer Vision and Pattern Recognition*, pages 4085–4095, 2020. 1

[39] Shuang Yu, Di Xiao, Shaun Frost, and Yogesan Kanagasingam. Robust optic disc and cup segmentation with deep learning for glaucoma detection. *Computerized Medical Imaging and Graphics*, 74:61–71, 2019. 5, 6, 7

[40] Jianpeng Zhang, Yutong Xie, Yong Xia, and Chunhua Shen. DoDNet: Learning to segment multi-organ and tumors from multiple partially labeled datasets. In *Proceedings of the IEEE/CVF Conference on Computer Vision and Pattern Recognition*, pages 1195–1204, 2021. 1

[41] Le Zhang, Ryutaro Tanno, Kevin Bronik, Chen Jin, Parashkev Nachev, Frederik Barkhof, Olga Ciccarelli, and Daniel C Alexander. Learning to segment when experts disagree. In *International Conference on Medical Image Computing and Computer-Assisted Intervention*, pages 179–190. Springer, 2020. 3

[42] Le Zhang, Ryutaro Tanno, Mou-Cheng Xu, Chen Jin, Joseph Jacob, Olga Ciccarelli, Frederik Barkhof, and Daniel Alexander. Disentangling human error from ground truth in segmentation of medical images. *Advances in Neural Information Processing Systems*, 33:15750–15762, 2020. 3, 6, 7

[43] Qinming Zhang, Luyan Liu, Kai Ma, Cheng Zhuo, and Yefeng Zheng. Cross-denoising network against corrupted labels in medical image segmentation with domain shift. In *Proceedings of the International Joint Conference on Artificial Intelligence*, 2020. 2

[44] He Zhao, Huiqi Li, and Li Cheng. Improving retinal vessel segmentation with joint local loss by matting. *Pattern Recognition*, 98:107068, 2020. 2